

Chapter 2

Field Ion Microscopy

Field ion microscopy, often referred to as FIM, provides atomic-resolution imaging of the surface of a specimen. A rare gas, called the imaging-gas, is introduced in the vicinity of a positively charged sharp needle. The electric field at the apex of the specimen is of the order of 10^{10} V m^{-1} . Gas atoms are ionised very close to the tip surface and subsequently accelerated away by the intense electric field. The image that is formed by the impact of these gas ions onto a phosphor screen maps the distribution of the electric field at the surface, which is intrinsically related to the local topography of the tip [1, 2]. The specimen is maintained at an extremely low temperature (5–80 K) to optimise the spatial resolution, which is high enough to provide direct imaging of individual surface atoms.

Further increasing the electric field at the surface of the tip induces the ionisation and desorption of atoms from the specimen itself via a process known as field evaporation. Successively removing layers of atoms from the surface of specimen enables the visualisation of the sub-surface structure of the specimen by using FIM.

Several comprehensive reviews and textbooks have been compiled on the development and application of FIM in materials and surface sciences [3–8]. The aim of this chapter is to give a brief overview of the physical principles as well as a practical explanation of how it functions.

2.1 Principles

FIM relies on the electric-field-induced ionisation of inert gas atoms in the vicinity of a charged surface. When a very sharp metallic needle is subjected to a high voltage of a few kilovolts, an intense electric field is generated at the surface. This electric field is generated by the positive charges present at the surface. Indeed, the application of the high voltage induces the free electrons to be, on average, displaced inwards by a small amount to screen the electric field, leaving partly charged atoms at the very surface. For a non-flat surface, protruding atoms are

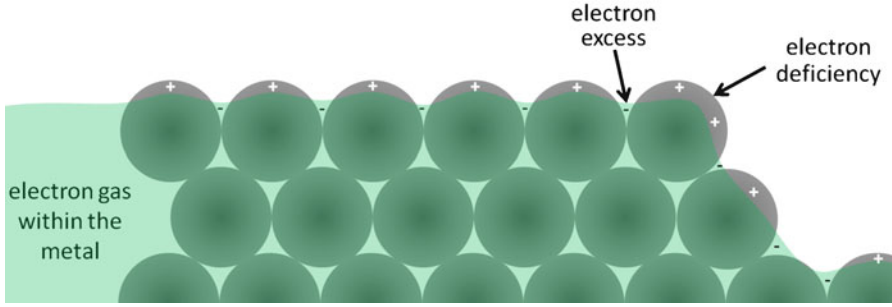


Fig. 2.1 Schematic view of the surface of a positively charged metal

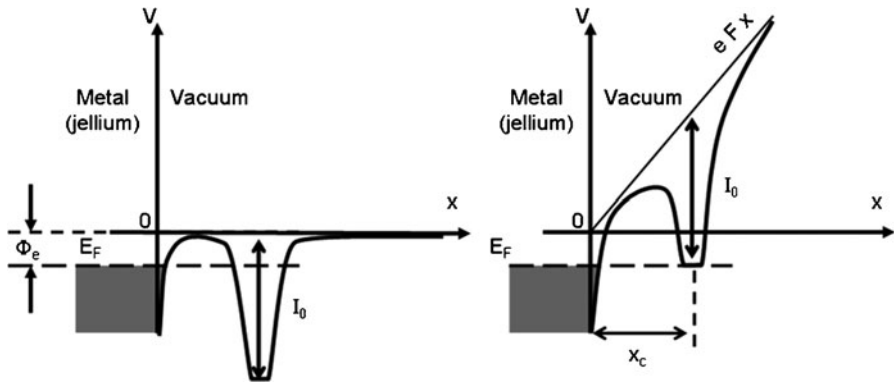


Fig. 2.2 Potential energy diagram as a function of the distance to the surface (x) of an electron from a gas atom in the vicinity of a tip (*left*) in the absence of an electric field, and (*right*) subject to an applied electric field, F . The energy of the first ionisation is I_0 , x_c is the critical distance of ionisation, E_F is the Fermi energy and Φ_e is the work function of the surface

subject to a greater charge, as shown in Fig. 2.1. Since the electric field at the surface is directly proportional to the charge density, it is higher around these local protrusions. In the case of an atomically smooth curved surface, these protrusions correspond to the edges of atomic terraces. By imaging the distribution of the field intensity at the surface, the field ion microscope provides an atomically resolved image of the surface itself. The fundamental aspects of FIM are detailed in the following sections.

2.1.1 Theory of Field Ionisation

Field ionisation is the field-induced removal of an electron from an atom. Figure 2.2 schematically presents the potential energy level of a gas atom in the vicinity of a metal surface in the absence or presence of an electric field. The electric field

polarises the gas atom, deforming the potential curve. When subjected to a very strong electric field, an electron from the outer shell of the gas atom can tunnel through the energy barrier towards an empty energy level at the metal surface. The probability of ionisation depends on the relative transparency of the potential barrier to the electron tunnelling process. The most widely accepted theoretical model used to describe this energy barrier was developed by Gomer [9], and assumes that the barrier can be modelled as an equilateral triangle. The width of the barrier is then proportional to the electric field, and thus, the ionisation probability is critically dependent on the amplitude of the electric field. Field ionisation will occur as close as possible to the surface, where the electric field is most intense.

However, the energy of the electron from the gas atom must coincide with, or be higher than, the lowest available conduction level in the metal, which is close to the Fermi level. If this condition is not fulfilled, there are no vacant energy levels in the metal available for the tunnelling electron [1, 6, 7, 9–14]. As a result, this process can only take place when the gas atom is beyond a critical distance away from the surface. To a first approximation, the critical distance can be written as:

$$x_c = \frac{I_0 - \Phi_e}{eF},$$

where I_0 is the energy of first ionisation, Φ_e is the work function of the surface, and F is the electric field. In the case of a helium atom ($I_0 = 24.59$ eV) ionised at 50 V nm^{-1} in the vicinity of a pure tungsten surface, where the work function is typically ~ 4.5 eV, this distance corresponds to approximately ~ 0.4 nm [11]. Hence, ionisation mostly takes place at this distance from the surface and, as shown by Müller and Bahadur [15], within a thin zone of thickness smaller than $0.1x_c$.

2.1.2 “Seeing” Atoms: Field Ion Microscopy

FIM is a direct and elegant application of field ionisation theory. In FIM, an imaging-gas is introduced into a vacuum chamber containing a sharp needle-shaped tip under a high positive electrical potential. The gas atoms or molecules are polarised by the intense electric field, and subsequently are electrostatically attracted towards the tip surface [12, 13]. The enhancement of the electric field in the vicinity of the tip draws in a high concentration of imaging-gas atoms (Fig. 2.3). The gas atoms strike the tip and bounce back and forth on its surface, losing some of their kinetic energy with each interaction [16]. This energy is transferred to the lattice in a process that may be viewed as a thermal accommodation of the gas atoms prior to their ionisation. In the best-case scenario, the energy of the gas atoms will be diminished to a level as low as the thermal energy of the tip’s surface. As the kinetic energy of the gas atoms progressively decreases, there is a corresponding decrease in their velocity, which in turn increases the time spent by the atoms in the ionisation zone, around the critical distance above the surface of the tip.

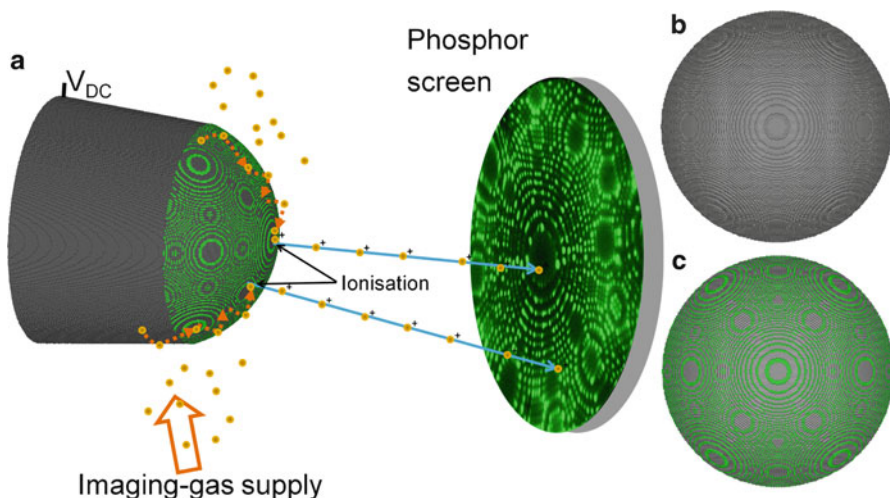


Fig. 2.3 Schematic view of a field ion microscope (not to scale). (a) Only the atoms from the very last shell (in *green*) of the tip surface can be imaged, as seen in the example of a pure W field ion micrograph (*right*). (b) Equivalent model of stacked spheres arranged on a bcc-lattice. (c) Similar view, with the most protruding atoms highlighted in *green*

Hence, the imaging-gas atoms will execute series of hops on and around the tip surface, with each hop diminishing their energy more than the previous, until ionisation finally occurs [13]. These new positively charged gas ions now experience the electric field force from the highly positive potential of the tip. As a result, they are repelled from the tip surface on a trajectory that is remarkably close to normal to the tangent of the specimen surface. The gas ions accelerate away from the tip through the microscope chamber and eventually strike a screen with a detection system, providing a vastly magnified projection of the specimen surface—a field ion micrograph.

This process is schematically represented in Fig. 2.3. A body-centred cubic (bcc) crystalline tip is shown side-on in Fig. 2.3a with gas atoms bouncing on and off the tip surface under the field polarisation force. The gas atoms are eventually accommodated at crystal ledge and terrace sites before being ionised and field evaporated off the surface. They are then accelerated towards the screen where an image is formed. Figure 2.3b, c depicts the physical origins of FIM images. A clear pattern made of series of concentric rings appears in (b), which is simply a top view of the model specimen shown side-on in (a). In (c), the most protruding atoms, being those farthest from the centre of the spherical cap, are highlighted in green. The resemblance to the micrograph in (a) is striking. It is clear that atomic resolution is achieved and that the image resembles the stereographic projection of the crystal. The crystal symmetry is retained and so (e.g.) the two-fold symmetry of the {110} planes that are oriented normal to the tip axis is also observed in the FIM image. Example FIM images are provided in Fig. 2.4a–i.

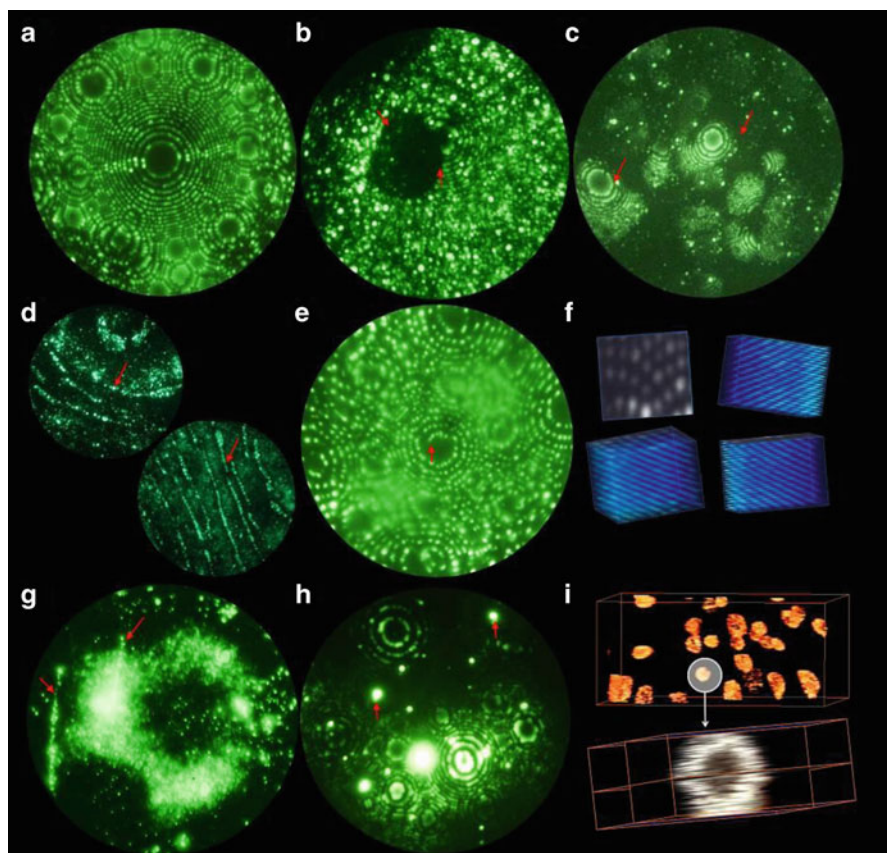


Fig. 2.4 Typical field ion micrographs from a variety of materials. (a) Pure W observed along the $\{110\}$ direction. (b) Darkly imaging precipitate in a $\text{Cu}_{81}\text{Fe}_9\text{Ni}_{10}$ alloy, the precipitate is coherent with the matrix as assessed by the continuity of the atomic terraces through the precipitate (red arrows). (c) Nanocrystals of pure Al (red arrows) in amorphous $\text{Al}_{92}\text{Sm}_8$ alloy, the matrix is amorphous and hence does not exhibit the typical pole structure. (d) Nitrided $\text{Fe}_{3\%}\text{Cr}$ alloy containing FeCrN platelets (red arrows) either observed from the top or edge-on. (e) Dislocation in pure Fe (red arrow). (f) reconstructed lattice in a pure Fe specimen observed by three-dimensional FIM. (g) Brightly imaging T1 platelets (red arrows) in observed side-on in an Al-Cu-Li-(Mg)-(Ag) alloy. (h) (Sc,Zr)-rich dispersoids (red arrows) in an Al-Zr-Sc alloy. (i) Same particles as in (h) observed by three-dimensional FIM: the core-shell structure of the precipitates is readily apparent (micrographs (a-f) and (h, i) courtesy of Drs Frederic Danoix, François Vurpillot and Williams Lefebvre)

2.1.2.1 Generation of the electric field

Field ionisation theory requires a high positive voltage in order to induce a high electric field at the surface of the sample. This is achieved by using a needle-shaped tip geometry for the specimen, with an end radius smaller than 100 nm. The shape of the tip is generally modelled as a truncated cone with a hemispherical cap,

although slight deviations from sphericity are generally encountered. The half angle at the apex of the cone is referred to as the *shank* or *taper angle* of the tip. The radius of the hemisphere is considered to be the *radius of curvature* of the tip. The electric field, F , generated at the apex of a needle-shaped specimen with a radius of curvature, R , that is subjected to a high voltage, V , can be estimated based on the idealised expression for a charged sphere. It does require slight modification to account for the fact that the tip is not exactly spherical, giving:

$$F = \frac{V}{k_f R},$$

where k_f is referred to as the *field reduction factor* or more simply *field factor* and is a constant that accounts for both the tip shape and its electrostatic environment [9]. Based on experimental studies of the energy distribution of ions created in the vicinity of a tip, Sakurai and Muller [17, 18] have shown that the field factor can range from 3 to 8 for tungsten tips. A smaller shank angle will increase the concentration of the field at the tip apex, resulting in a decrease in k_f [19].

Larson et al. observed that k_f varies almost linearly with the shank angle [19] in FIM. This is in relatively good agreement with calculations by Gipson et al. [20–22]. The field factor has been shown to be influenced by the value of the radius of curvature and by the overall shape of the specimen [20, 21, 23, 24]. Furthermore, other parameters, which are independent of the tip shape itself, impact the value of the field factor. For example, the presence of a flat substrate underneath the specimen, positioned too close to the apex, causes a dramatic drop in the field; conversely, the presence of a counter-electrode close to the tip apex increases the electric field: a decrease in k_f of more than a factor of two has been experimentally observed as a result of changing the distance between the counter-electrode and the specimen [20–22, 25].

The specimen is not only subjected to a high electric field but also cooled down to cryogenic temperatures, which leads, for multiple reasons, to an improved spatial resolution. First, at lower temperature, the thermal agitation of the surface atoms is reduced. Furthermore, diffusion of the atoms from the specimen across its surface is a thermally activated process, which can be if not completely avoided, at least greatly minimised at cryogenic temperatures, increasing confidence that the surface atoms are observed in their original positions and have not been redistributed by the electric field. Another critical purpose of the cryogenic temperatures is to provide *thermal accommodation* of the imaging-gas atoms. Reducing the thermal energy, $k_B T$, of the imaging-gas atoms has the effect of lowering their lateral velocity at the instant of their evaporation, thereby increasing the spatial resolution as is discussed further below [7, 26, 27].

2.1.2.2 Projection of the Ions: Formation of the Image

Once ionised, the imaging-gas atoms are affected by the very intense electric field surrounding the tip. The electric field accelerates the ions as they are repelled from

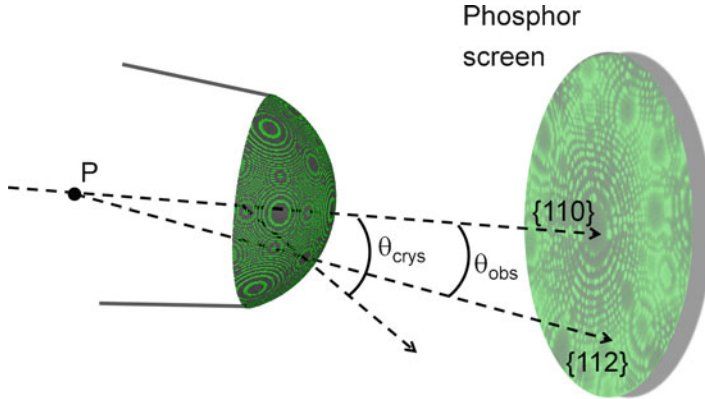


Fig. 2.5 Schematic view of the point-projection of the atoms from the surface

the tip surface. As the electric field is nearly normal to the surface, the ions fly along the electric field lines and behave as if they are projected away from the surface. Several models have been proposed to describe the ion projection [28–32]. The most widely used, although not necessarily the most accurate model [29, 30, 33], is a point-projection. By placing a screen at a distance L from the tip, typically a few centimetres, the magnification, M_{proj} , of the image formed by the impact of the ions can be expressed as [34]:

$$M_{\text{proj}} = \frac{L}{\xi R},$$

where R is the radius of curvature of the tip and ξ is a constant called the *image compression factor* (ICF). Similarly to the field factor that accounted for a combination of effects, the ICF accounts for the deflection of the field lines towards the specimen main axis linked to the specimen shape and its electrostatic environment altogether. The ICF can be seen as the ratio between the observed angle θ_{obs} between two crystallographic directions on the projected image and the theoretical value θ_{crys} , as defined in Fig. 2.5:

$$\xi \approx \frac{\theta_{\text{crys}}}{\theta_{\text{obs}}}.$$

The ICF (ξ) typically ranges between 1 (radial projection) and 2 (stereographic projection). In many studies, ξ has been shown to lie somewhere near the middle of these two figures [28, 33]. For typical values of $L = 90$ mm, $\xi = 1.5$ and $R = 50$ nm, a magnification higher than 10^6 is reached, enabling the resolution of the positions of the individual atoms.

Upon impact on the phosphor screen, each ion produces a spot of light, as seen in Fig. 2.3. The overall image is the culmination of light spots from atoms ionised over

the entire surface of the specimen. Importantly, although the field ion image can seem to be static, its formation is actually a dynamic process, whereby each bright region of the image is formed by a continuous flow of ionised imaging-gas originating from the ionisation zone, just above the protruding atoms. Brighter spots on the image correspond directly to zones where a higher ion current is produced.

2.1.3 *Spatial Resolution of FIM*

Despite being crucial to understanding the intrinsic limitations of a technique, the concept of resolution in microscopy has still not been unambiguously defined, leaving room for interpretation. Microscopes have limited capabilities to image a given feature, which translates into a finite resolution. Deformations induced by the microscope itself (i.e. aberrations) are generally put in the form of a point-spread function that describes the response of the microscope to an individual point. The point-spread function can then be exploited to deduce the resolution limit. The latter is generally deduced from well-established criteria, such as the classic Rayleigh's criterion, to provide values of the so-called two-point resolution, which is the microscope's ability image two individual points of equal intensity. This is a widely used approach to assess the resolving capabilities of a microscope.

Definitions in FIM often relate to the size of the smallest image spot on the screen, which corresponds to the point-spread function. Based on the pioneering work of Chen and Seidman [26] or de Castilho and Kingham [27], Tsong [7] proposed a model based on three major factors to describe the origins of the resolution limit of FIM:

- *The size of the ionisation zone.* As each spot is formed by the successive impact of a continuous flow of ions projected onto the detector, its size will correspond to the lateral size of the ionisation zone directly above the image atom on the tip surface.
- *Lateral velocity.* Trajectory aberrations, originating from the lateral velocity of the ions at the instant of their field ionisation, contribute to the increase in the spot size.
- *Positional uncertainty.* The gas atom is confined in a very small volume, and hence, the quantum nature of the atom must be considered. The Heisenberg's uncertainty principle imposes a spread in the lateral velocity component of the imaging-gas atom. This introduces an uncertainty in its position.

2.1.3.1 **Ionisation Zone**

The lateral expansion of the ionisation zone above the imaged atom is difficult to quantify. In the best case, it is of the same order of magnitude as the size of the imaging-gas atom. However, it is critically dependent on the amplitude and distribution of the electric field above the atom. If the field is relatively low, the critical distance x_c will be large, and hence, the field distribution in the ionisation

zone may not reflect the structure on the surface with atomic resolution. Conversely, if the electric field is too high, the ionisation zone will be closer to the surface and its lateral extent above a specific surface atom will overlap with the zones of that atom's neighbours. Such effects blur the image. Thus, the definition of the *best image field* (BIF) is the field for which the volume of the ionisation zone is minimal and which results in the highest resolution.

2.1.3.2 Lateral Velocity

Ions are formed when the gas atoms are hopping through the ionisation zone near the surface. Therefore, their velocity has a component parallel to the tip surface that depends on their kinetic energy. This kinetic energy depends on the tip's temperature and can be estimated if the gas is considered to be ideal. After field ionisation, the imaging-gas ion is projected from the vicinity of the tip onto the screen. If the ions generated above a single atom exhibit a statistical distribution in their initial lateral or tangential velocity, they will not all follow the exact same trajectory. Such trajectory aberrations induce a spread of the ion impact position on the screen. The image of a single point in the ionisation zone is hence no longer a single point but a spot. The amplitude of these trajectory aberrations therefore is also linked to the projection properties of the tip itself (i.e. radius of curvature, image compression factor, etc.).

2.1.3.3 Heisenberg's Uncertainty

One must also consider the spread in the tangential velocities due to the confinement of the imaging-gas. The Heisenberg uncertainty principle states that the position and energy of the atom cannot be precisely determined at the same time. The *de Broglie* wavelength of a helium atom, due to its thermal agitation at 20 K, is on the order of 0.2 nm, bigger than the size of the zone in which the atoms are ionised. The quantum nature of the atom therefore cannot be neglected. This effect will be much less noticeable in FIM than in field electron emission microscopy, as ions are much heavier than electrons and their wavelengths are significantly smaller. This lateral velocity will also contribute to the broadening of the ion trajectories that exit from above a particular atomic site.

2.1.3.4 Resolution

An equation has previously been derived to describing the resolution δ of the instrument. It contains three terms, related to these different limiting factors, and can be written as:

$$\delta = \left\{ \delta_0^2 + 16 \left(\frac{\xi^2 k_B T R}{k_f e F} \right) + 4 \left[\frac{\xi^2 \hbar^2 R}{2 m k_f e F} \right]^{1/2} \right\}^{1/2},$$

where δ_0 is the size of the ionisation zone, ξ is the image compression factor, k_B is the Boltzmann constant, T is the temperature of the imaging-gas atom immediately before ionisation, R is the tip radius, k_f is the field factor, e is the elementary charge, F is the electric field at the tip apex, \hbar is the Planck constant and m is the mass of the imaging-gas atom.

In summary, the resolution, as described by the above equation, is limited by the size of the ionisation zone (first term), its lateral velocity at the moment of ionisation (second term), and the Heisenberg uncertainty (third term). Temperature has a strong effect on the third term, and thus should be kept as low as possible to ensure the best possible resolution. A higher electric field and smaller tip radius also improve resolution. By using the proposed definition, the best resolution achievable in FIM is about 0.2 nm with He at 20 K.

2.2 Instrumentation and Techniques for FIM

2.2.1 FIM Instrumentation

Figure 2.6 shows the key components of instrumentation for FIM. The instrument consists of an ultra-high vacuum chamber, which is required to operate at a base pressure below 10^{-8} Pa ($\sim 10^{-10}$ Torr). This is achieved through the use of high-compression-rate turbo-molecular pumps backed by rotary pumps. Low specimen temperatures must be maintained to achieve high resolution. Early microscope designs simply used liquid nitrogen, hydrogen or helium to cool the specimen [35]. Since the 1980s, closed-cycle helium cryostats have generally been used to reach temperatures below 20 K. A high-voltage DC power supply is connected to the specimen in order to generate the required electric field. Once the tip is positioned and thermally stabilised, a very low pressure, in the range of 10^{-3} to 10^{-4} Pa ($\sim 10^{-5}$ to 10^{-6} Torr), of imaging-gas is introduced into the chamber. The most commonly used gases are He and Ne, although in some cases H_2 has also been used. Multiple gases in combination can also be used to resolve images from several phases at the same time [13, 36].

The FIM screen is composed of a stack of biased micro-channel plates (MCPs), which is used as an image intensifier, placed immediately in front of a phosphor screen. A MCP consists of an array of tiny glass tubes with a diameter of the order of a few tens of microns, covered by a thin conductive layer [37]. The tubes are oriented at an angle of approximately $15\text{--}5^\circ$ to normal. Generally, one of the faces of the MCP is biased at about -1 kV, creating a high surface charge density. The opposite side is grounded, which induces an electric field between the two faces. When a particle, ion, electron or photon hits the inside wall of one of the tubes, secondary electrons are emitted by the surface. By virtue of the electric field, they are driven towards the back face. Each time one of these electrons collides with the wall of the tube, another cluster of secondary electrons is ejected, ultimately

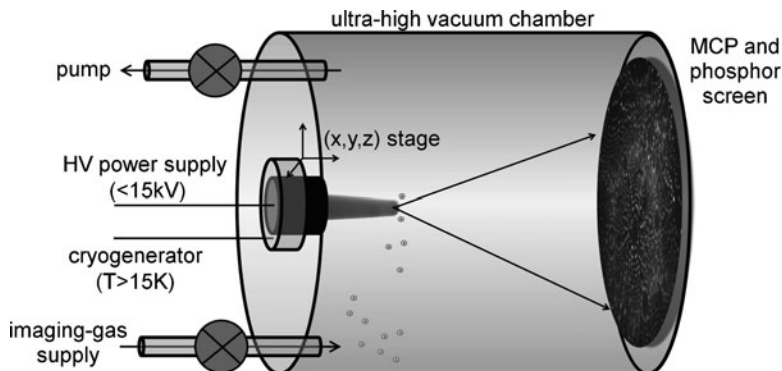


Fig. 2.6 Experimental setup of a field ion microscope

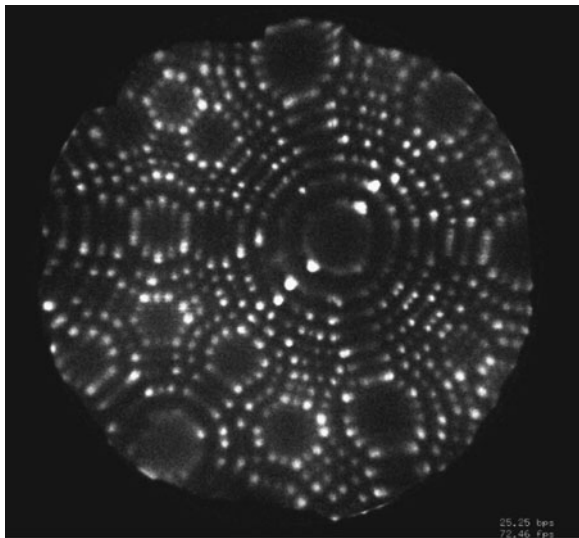
producing a cascade of several thousand electrons for each corresponding ion that impacts the surface. The electrons are consequently focussed onto the phosphor by an electric field imposed between the MCP and the phosphor screen, which produces a spot of light on impact of the electrons.

The detection-efficiency of the MCP can be defined as the probability that it will successfully detect a single ion striking its surface. This detection-efficiency is theoretically limited by the open area of the MCP, i.e. the fraction of the surface area of the detector that serves as an opening to the micro-channels. This fraction has an approximate value of between 50% and 60%. However, in the case of FIM, high number of imaging-gas ions contributes to form a single spot within the image. Indeed even if 50% of the ions reaching the MCP are not detected, there will still be thousands of ions that are successfully detected and will contribute to the formation of each spot. Hence, the detection-efficiency limitation imposed by the MCPs is not a significant issue in FIM. Other design issues can also affect the efficiency of the MCPs. For example, a zone of lower efficiency can still generally be observed due to the angle between the micro-channels and the surface. An ion flying at exactly the same orientation as the MCP micro-channels will pass directly to the bottom of the channel without hitting the wall and therefore will not provoke an electron cascade. Early designs of field ion microscopes were not equipped with MCPs. Instead, images were recorded by acquiring the light emitted by the phosphor screen onto photographic plates over up to several minutes, or used external image amplification devices.

2.2.2 *eFIM or Digital FIM*

These methods involve the detection of the imaging-gas ions using delay-line detectors such as those employed in contemporary atom probe tomography. These detectors are capable of collecting and treating a very large number of atoms

Fig. 2.7 e-FIM of a pure W specimen imaged at 20 K, 3.5 kV in He



and therefore FIM experiments can be digitally recorded at data collection rates of about 10^6 ions per second. Corresponding FIM images can then be simulated by modelling the response of a virtual phosphor screen to each single event detected [38].

Various settings can be tuned, such as the contrast, brightness, gamma, integration time and the simulated decay of the phosphor response, to improve the image quality or reveal particular features. Contrast sufficient to observe nearly every surface atom can be achieved just as in traditional FIM, as shown in Fig. 2.7, although the quality of the image is generally slightly lower. Using the same detector enables iterative APT and FIM experiments to be performed more easily on the same specimen. As the two techniques can reveal different information from the specimen, coupling these two approaches can be beneficial.

2.2.3 Tomographic FIM Techniques

In FIM, the specimen is most often field evaporated, which, as described in the Chap. 3, provides a mean to investigate the depth of the specimen. Provided that the specimen is field evaporated at a constant rate, the in-depth distance between successive images taken at regular time intervals remains constant. Exploiting this principle, the 3D FIM [39] or Computed Field Ion Image Tomography [40] simply involves stacking a sequence of field ion images recorded by a high-resolution CCD (charge-coupled device) camera. A tomographic image is ultimately produced, as shown in Fig. 2.4f, i. Similar tomographic reconstruction of the imaged volume could be achieved in eFIM, as the individual impact positions of

the imaging-gas atoms are stored. No such attempt has yet been reported. Initial attempts to correct the volume to account for the curvature of the tip have not systematically been meticulously pursued [39, 41], and thus, artefacts can appear in the tomographic volume.

In the tomographic FIM data, it is possible to observe transversal slices, or sub-volumes revealing details of the crystal structure (Fig. 2.4f). In the dataset, each atom is represented by an elongated ellipsoid. Although no actual work has been undertaken to evaluate the performance of the technique, it can be assumed that the length of the ellipsoid is roughly equivalent to the lateral resolution of the FIM (~ 0.3 nm in [39]), while its thickness approximates the in-depth resolution. The latter depends on the average time an atom remains on a site that can be imaged, and thus should depend on the evaporation rate (~ 0.05 nm in [39]). Finally, by virtue of the elemental contrast, different features can be imaged and their orientation, number density and/or average shape can be determined.

2.3 Interpretation of FIM Images

With an imaging efficiency of nearly 100%, FIM enables the visualisation of crystallographic defects such as vacancies, dislocations (see Fig. 2.4) or grain boundaries. Furthermore, a difference in contrast between species or phases enables their observation. During FIM analysis the specimen is generally progressively field evaporated to reveal its internal structure and hence careful analysis of successive images recorded from the same specimen can provide three-dimensional information on these various features in the bulk of the specimen. As seminal reviews or textbooks already exist on FIM and its application in materials sciences [4, 6, 7], this section first describes the basics of field ion micrograph interpretation and subsequently only focuses on selected applications of the FIM that can be usefully correlated to results obtained by atom probe tomography.

2.3.1 *Interpretation of the Image in a Pure Material*

Figure 2.8a presents an example of a FIM image from a pure aluminium specimen oriented with the [001] direction pointing towards the detector. This field ion micrograph compares well with a stack of small spheres arranged in the form of a spherical cap shown in Fig. 2.8b. The bright spots in the FIM image correspond to the green atoms in the model, which are those located on the outermost shell of the hemisphere at the end of the tip, and are thus the atoms that protrude the most at the surface [42, 43]. In the case of crystalline materials, the image generally displays concentric rings. Each of these assemblies of rings corresponds to a set of major crystallographic planes protruding at the surface and is called a pole. The contrast of each atom appears to be linked to the actual number of close neighbours in the

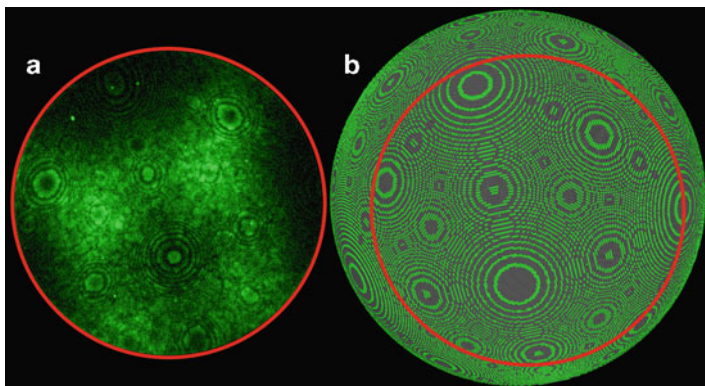


Fig. 2.8 (a) He eFIM of pure Al observed on a Cameca LEAP 3000X Si at 24 K under an applied voltage of 12.5 kV. The specimen is approximately oriented along the [001] direction. (b) Shows a spherical tip apex modelled as a stack of small spheres (ball model) in a FCC arrangement. The most protruding atoms are represented in green. The red circle highlights the actual field-of-view

vicinity of each kink-site atom (i.e. each protruding atom at the edge of a plane). It is clear that FIM images contain broad variations in brightness. For example, in Fig. 2.8a large bright regions are formed. These linear zones of higher field are generally called zone lines, and they appear to link poles.

The pattern of poles and zone lines is in fact the result of the accommodation of the crystal lattice to an equilibrium shape during field evaporation, which, to a first approximation is often considered as quasi-hemispherical. This leads to a surface made of a complex combination of facets formed around major poles. The position and size of these facets are directly dependent on the corresponding crystallographic direction, as, for example, the work function and vary from direction to direction, the intensity of the electric field and the temperature. Zone lines form at the boundary between these facets. Finally, the image has similarities to a stereographic projection of the corresponding crystal structure [29, 31, 33], such that for cubic crystals where crystallographic directions are normal to the planes, directions can be directly identified. The symmetry relative to each specific direction helps with the process of identifying the poles. Potential uses of identifying these poles will be discussed later in Sect. 2.3.3.4 and in Chap. 7. The stereographic projections included in Appendix F can be of great help to identify the different poles.

2.3.2 Interpretation of the Image for Alloys

In the case of alloys, contrast generally exists between different chemical phases and atoms of different elements. Two main reasons have been proposed to explain this contrast. The first reason is that atoms of different species present at the surface of the material have different affinities to the imaging-gas atoms, leading to

variations in charge transfer. Thus, selective ionisation above certain atoms could occur, leading to brighter spots on the image where these specific atoms are positioned [6].

The second reason relates to changes in the local curvature of the tip. During a FIM experiment, the tip is progressively field evaporated. The electric fields required for field evaporation are specific to each species. The tip is subjected to a high-voltage, and to enable the departure of a given type of atom, the local curvature of the tip has to evolve to reach the evaporation field of this element. For example, if the evaporation field of the solute or of a precipitate is lower than that of the matrix, these atoms will generally appear dark on the image, as shown in Fig. 2.4b, as the local curvature will be smaller and hence the field lower. In contrast, a solute atom with a higher evaporation field will appear bright. This is demonstrated in the field ion micrograph shown in Fig. 2.4d, g–h, where Cu-rich or (Sc,Zr)-rich particles appear much brighter than the surrounding aluminium matrix. These local variations in curvature are responsible for aberrations in the trajectories of the imaging-gas ions, as well as for ions field evaporated from the tip, a problem that is discussed further in Chap. 7, as it similarly impacts atom probe tomography.

2.3.3 *Selected Applications of the FIM*

2.3.3.1 Orientation

The first generations of three-dimensional atom probes were only able to analyse a very limited area of the specimen surface. FIM was generally performed prior to any atom probe analysis in order to clean the tip surface and reveal the crystallographic orientation of the specimen or the position of a particular feature, such as a grain boundary, precipitate, or a specific phase, that could subsequently be analysed by atom probe.

2.3.3.2 Radius of Curvature

In atom probe tomography, when atomic planes can be observed in the tomographic reconstruction, the interplanar spacing can be used to calibrate the dimensions of the reconstruction [44]. However, it is first necessary to identify the corresponding crystallographic direction, which is not always straightforward, especially when only a limited area of the surface is imaged. In FIM, a wide area over the tip surface is normally imaged and several poles can usually be observed. Since the symmetries of the crystal are more apparent, the poles can be much more readily identified. Although the advent of wide-angle atom probes has made this process less necessary, other important information can still be obtained.

Indeed, the pattern of concentric rings observed in FIM images relates to the local geometry of the tip. Exploiting the image can enable the determination of, for

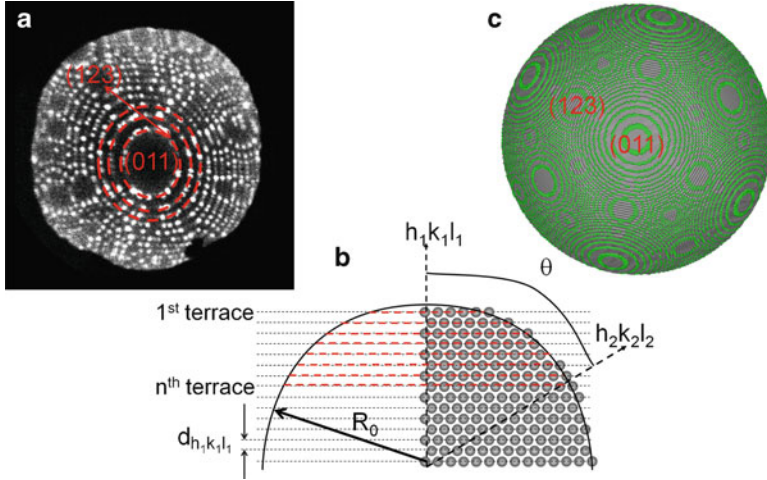


Fig. 2.9 (a) eFIM image of a pure tungsten specimen, in which the *dashed line circles* highlight some of the successive terraces between the [011] and [123] directions. (b) Schematic view of the tip apex and (c) corresponding ball model

example, the radius of curvature or shank angle of the tip. Each of the successive terraces between two poles on a FIM image (Fig. 2.9a) correspond to an increment equal to the interplanar spacing along the direction of this pole; see Fig. 2.9b. It is therefore possible to establish a relationship between the angle, θ_n , between two crystallographic directions $h_1k_1l_1$ and $h_2k_2l_2$ and the radius of curvature of the tip R_0 :

$$R_0(1 - \cos \theta_n) \approx nd_{h_1k_1l_1}.$$

Both local and global radii of curvature can be determined using this method [29].

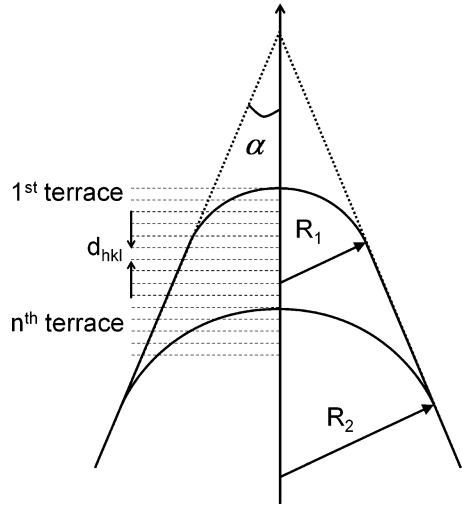
2.3.3.3 Shank Angle

The evolution of the radius of curvature while the tip is progressively field evaporated is determined by the geometry of the shank angle. As illustrated in Fig. 2.10, by estimating the radii of curvature, R_1 and R_2 , at two stages separated by a known number, n , of atomic terraces along the hkl direction, the shank angle, α , can be determined, from the geometrical relationship:

$$\sin(\alpha) = \frac{R_2 - R_1}{R_2 - R_1 + nd_{h_1k_1l_1}},$$

where d_{hkl} is the inter-atomic spacing between the hkl planes. Strictly speaking, this method enables the determination of the half-shank angle, which is often simply called shank angle.

Fig. 2.10 Evolution of the radius of curvature with the geometry of the tip



2.3.3.4 Image Compression Factor

As introduced in Sect. 2.1.2.2, the magnification of the image is affected by the modification of the field lines due to the shape of the tip and its electrostatic environment. The image compression factor can be expressed as the ratio of the crystallographic to observed angles, $\xi \approx \theta_{\text{crys}}/\theta_{\text{obs}}$, where θ_{obs} is the observed angle between two crystallographic directions on the projected image and θ_{crys} the theoretical value, as shown in Fig. 2.11. The radius of the tip is negligible compared to the flight path L , so the observed angle can be written as:

$$\theta_{\text{obs}} = \arctan \frac{D}{L},$$

where D is the distance between the centres of the two poles on the image. The theoretical angles between crystallographic directions are defined by the structure and can be easily calculated by using the formulas provided in Appendix E.

2.3.3.5 Surface-Diffusion Processes

Atoms adsorbed on a surface can undergo a thermally activated process of *random walk* [45, 46] whereby an atom jumps from one location to another across the specimen surface. The excellent spatial resolution of FIM [26] makes it a unique tool to investigate such processes, and hence extensively studies have been undertaken over the years.

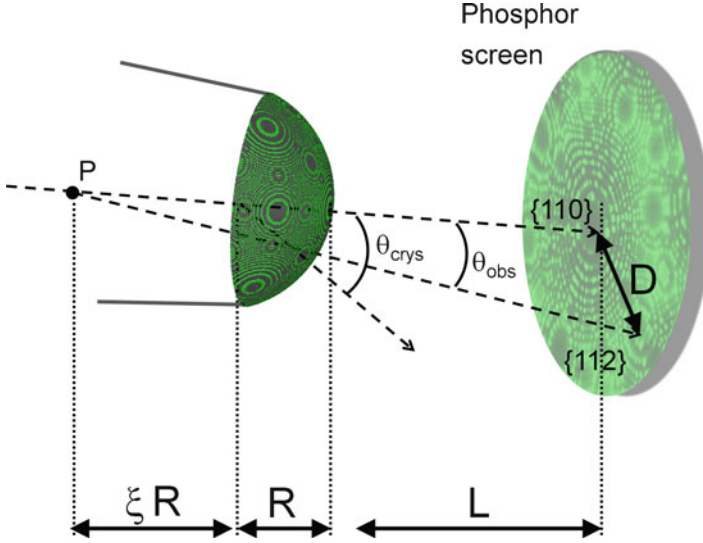


Fig. 2.11 Determination of the image compression factor

Similar to field evaporation, surface diffusion is a thermally assisted process that can be described by the Arrhenius law:

$$N_{\text{diff}} = v_0 \exp\left(-\frac{Q_{\text{diff}}}{k_B T}\right),$$

where N_{diff} is the number of hops from one site to another per second and v_0 the surface atom vibration frequency. The activation energy of surface diffusion Q_{diff} can be estimated by measuring the mean square displacement $\langle \rho^2 \rangle$ of a surface atom as a function of the emitter temperature:

$$\frac{\langle \rho^2 \rangle}{2\tau_0} = D_0 \exp\left(-\frac{Q_{\text{jump}}}{k_B T}\right),$$

where D_0 is the surface diffusivity and τ_0 is the time of observation. Specifically, FIM has been used to provide measurement of surface diffusion coefficients, using heat cycles to precisely control the rate of surface migration, or to garner insight into the formation and displacement mechanisms of atomic clusters on surfaces, which are relevant to materials fabrication via deposition processes. This research activity has been the subject of many detailed reviews [7, 45, 47, 48]. Further, surface migration measurements have been used to probe the temperature reached by the specimen during pulsed-laser irradiation [49, 50].

Surface diffusion processes are not restricted to adsorbed species. Indeed atoms belonging to the material can be subject to migration if sufficient thermal energy is

available. In the presence of an electric field, atoms on the surface become polarised. Due to the polarisation energy $((1/2)\alpha_p F^2)$, variations in the electric field influence the relative stability of different sites at the surface. In such a case migration of atoms subject to surface diffusion can no longer be considered a random process. Instead, atoms will preferentially migrate towards regions of higher electric field, a process generally referred to as a *directional walk* [51–53]. As surface diffusion and field evaporation are both facilitated by the electric field and are both thermally activated, there is a competition between these two processes, which has sometimes been considered as limiting the rate of field evaporated atoms from a surface [54, 55].

2.3.4 Summary

Most of the key parameters used within the tomographic reconstruction generated by atom probe tomography can be calibrated by using FIM: the radius of curvature and shank angle of the specimen, along with the image compression factor or field factor. FIM provides a unique way to estimate these parameters. However, it is important to keep in mind that what is observed by using FIM is not strictly an image of the surface itself, but rather an image of the ionisation zone located up to a few nanometres above the surface. This ionisation zone directly relates to the surface itself, but this distinction is enough to potentially introduce biases on measurements and observations. FIM still provides a unique technique to access these values. It also offers unparalleled spatial resolution for observation of surface processes and structure of the surface, but also, thanks to its new three-dimensional capabilities, of the bulk of a specimen, which makes FIM an invaluable tool for materials research.

References

1. E.W. Müller, J. Appl. Phys. **27**(5), 474–476 (1956)
2. E.W. Müller, Phys. Rev. **102**(3), 618–624 (1956)
3. K.M. Bowkett, D.A. Smith, *Field-Ion Microscopy* (North-Holland Pub. Co., Amsterdam, 1970)
4. M.K. Miller, A. Cerezo, M.G. Hetherington, G.D.W. Smith, *Atom Probe Field Ion Microscopy* (Oxford Science Publications - Clarendon Press, Oxford, 1996)
5. M.K. Miller, G.D.W. Smith, *Atom Probe Microanalysis: Principles and Applications to Materials Problems* (Materials Research Society, Pittsburg, PA, 1989)
6. E.W. Müller, T.T. Tsong, *Field Ion Microscopy, Principles and Applications* (Elsevier, New York, NY, 1969)
7. T.T. Tsong, *Atom-Probe Field Ion Microscopy: Field Emission, Surfaces and Interfaces at Atomic Resolution* (Cambridge University Press, New York, NY, 1990)
8. R. Wagner, *Field-Ion Microscopy* (Springer-Verlag, Berlin Heidelberg, 1982)
9. R. Gomer, *Field Emission and Field Ionisation* (Harvard University, Cambridge, 1961)

10. D.G. Brandon, *Philos. Mag.* **7**(78), 1003–1011 (1962)
11. D.G. Brandon, *Br. J. Appl. Phys.* **14**(8), 474 (1963)
12. E.W. Müller, *Acta Crystallogr.* **10**(12), 823–823 (1957)
13. E.W. Müller, *Science* **149**(3684), 591–601 (1965)
14. T.T. Tsong, *Surf. Sci.* **70**, 211 (1978)
15. E.W. Müller, K. Bahadur, *Phys. Rev.* **102**(3), 624–631 (1956)
16. E.W. Müller, S. Nakamura, O. Nishikawa, S.B. McLane, *J. Appl. Phys.* **36**(8), 2496–2503 (1965)
17. T. Sakurai, E.W. Müller, *Phys. Rev. Lett.* **30**(12), 532–535 (1973)
18. T. Sakurai, E.W. Muller, *J. Appl. Phys.* **48**(6), 2618–2625 (1977)
19. D.J. Larson, K.F. Russell, M.K. Miller, *Microsc. Microanal.* **5**, 930–931 (1999)
20. G.S. Gipson, *J. Appl. Phys.* **51**(7), 3884–3889 (1980)
21. G.S. Gipson, H.C. Eaton, *J. Appl. Phys.* **51**(10), 5537–5539 (1980)
22. G.S. Gipson, D.W. Yarnitell, H.C. Eaton, *J. Phys. D: Appl. Phys.* **12**(7), 987–996 (1979)
23. B. Gault, D. Haley, F. de Geuser, D.J. Larson, E.A. Marquis, B.P. Geiser, *Ultramicroscopy* **111**(6), 448–457 (2011)
24. B. Gault, A. La Fontaine, M.P. Moody, S.P. Ringer, E.A. Marquis, *Ultramicroscopy* **110**(9), 1215–1222 (2010)
25. M. Huang, A. Cerezo, P.H. Clifton, G.D.W. Smith, *Ultramicroscopy* **89**(1–3), 163–167 (2001)
26. Y.C. Chen, D.N. Seidman, *Surf. Sci.* **26**(1), 61–84 (1971)
27. C.M.C. de Castilho, D.R. Kingham, *J. Phys. D: Appl. Phys.* **20**(1), 116–124 (1987)
28. D.G. Brandon, *J. Sci. Instrum.* **41**(6), 373–375 (1964)
29. T.J. Wilkes, G.D.W. Smith, D.A. Smith, *Metallography* **7**, 403–430 (1974)
30. A. Cerezo, P.J. Warren, G.D.W. Smith, *Ultramicroscopy* **79**(1–4), 251–257 (1999)
31. M.A. Fortes, *Surf. Sci.* **28**(1), 117–131 (1971)
32. H.N. Southworth, J.M. Walls, *Surf. Sci.* **75**(1), 129–140 (1978)
33. R.W. Newman, R.C. Sanwald, J.J. Hren, *J. Sci. Instrum.* **44**, 828–830 (1967)
34. J.M. Walls, H.N. Southworth, *J. Phys. D: Appl. Phys.* **12**(5), 657–667 (1979)
35. R.G. Forbes, *J. Microsc. Oxford* **96**(Aug), 63–75 (1972)
36. A. Menand, T. Alkassab, S. Chambreland, J.M. Sarrau, *J. Phys.* **49**(C-6), 353–358 (1988)
37. J.L. Wiza, *Nucl. Instrum. Methods* **162**(1–3), 587–601 (1979)
38. R.M. Ulfing, D.J. Larson, S.S.A. Gerstl (unpublished, 2008)
39. F. Vurpillot, M. Gilbert, B. Deconihout, *Surf. Interface Anal.* **39**(2–3), 273–277 (2007)
40. C. Wille, T. Al-Kassab, A. Heinrich, R. Kirchheim, presented at the IVNC 2006/IFES 2006 (unpublished, 2006)
41. J. Akre, F. Danoix, H. Leitner, P. Auger, *Ultramicroscopy* **109**, 518–523 (2009)
42. A.J.W. Moore, *J. Phys. Chem. Solids* **23**(Jul), 907–912 (1962)
43. A.J.W. Moore, S. Ranganathan, *Philos. Mag.* **16**(142), 723–737 (1967)
44. J.M. Hyde, A. Cerezo, R.P. Setna, P.J. Warren, G.D.W. Smith, *Appl. Surf. Sci.* **76/77**, 382–391 (1994)
45. G. Ehrlich, K. Stolt, *Annu. Rev. Phys. Chem.* **31**, 603–637 (1980)
46. G. Antczak, G. Ehrlich, *Surf. Sci. Rep.* **62**(2), 39–61 (2007)
47. T.T. Tsong, *Prog. Surf. Sci.* **67**, 235–248 (2000)
48. G.L. Kellogg, T.T. Tsong, P. Cowan, *Surf. Sci.* **70**(1), 485–519 (1978)
49. G.L. Kellogg, *J. Appl. Phys.* **52**, 5320–5328 (1981)
50. F. Vurpillot, J. Houard, A. Vella, B. Deconihout, *J. Phys. D: Appl. Phys.* **42**(12), 125502 (2009)
51. T.T. Tsong, G. Kellogg, *Phys. Rev. B* **12**(4), 1343–1353 (1975)
52. S.C. Wang, T.T. Tsong, *Phys. Rev. B* **26**(12), 6470–6475 (1982)
53. J. Neugebauer, M. Scheffler, *Surf. Sci.* **287/288**, 572–576 (1993)
54. M. Wada, *Surf. Sci.* **145**, 451–465 (1984)
55. C.G. Sanchez, A.Y. Lozovoi, A. Alavi, *Mol. Phys.* **102**(9–10), 1045–1055 (2004)

Atom Probe Microscopy

Gault, B.; Moody, M.P.; Cairney, J.M.; Ringer, S.P.

2012, XXIV, 396 p., Hardcover

ISBN: 978-1-4614-3435-1